




## Extremely space- and time-limited phonon propagation from electron-lattice scattering induced by Sb/Bi codoping in $\text{Ge}_{0.86}\text{Sb}_{0.08}\text{Bi}_{0.06}\text{Te}$ single crystal

Ma-Hsuan Ma,<sup>1</sup> Chun-Min Wu,<sup>2</sup> Tsu-Yin Ling,<sup>1</sup> Erdembayalag Batsaikhan <sup>1</sup>, Wen-Hsien Li <sup>1,\*</sup>,  
Vankayala Krishna Ranganayakulu <sup>3,4</sup> and Yang-Yuan Chen<sup>3</sup>

<sup>1</sup>Department of Physics, National Central University, Zhongli 32001, Taiwan

<sup>2</sup>National Synchrotron Radiation Research Center, Hsinchu 30076, Taiwan

<sup>3</sup>Institute of Physics, Academia Sinica, Taipei 11529, Taiwan

<sup>4</sup>Department of Engineering and System Science, National Tsing Hua University, Hsinchu 30013, Taiwan



(Received 18 May 2021; accepted 18 October 2021; published 3 November 2021)

Phonon dispersions and linewidths of layered thermoelectric Sb/Bi codoped  $\text{Ge}_{0.86}\text{Sb}_{0.08}\text{Bi}_{0.06}\text{Te}$  covering 300 to 630 K in the  $R3m$  phase are mapped by inelastic neutron scattering measurement. The acoustic phonons depart greatly from the harmonic frequencies with downturns in dispersion revealing soft phonon energies at larger wave vectors for phonons propagating in the crystallographic [110] direction. Two components that scatter phonons are identified. One is smaller in magnitude having a linear wave vector  $q$  dependency that links to the three-phonon scattering. The dominant component for phonon softening has a wave vector square  $q^2$  dependency with a Fermi-Dirac thermal reduction rate linked to the electron-phonon scattering. The scattering of phonons is so strong that they only propagate over a few unit cells in length, with lifetimes as short as  $\sim 1$  ps. Our results reveal the origin of the extremely low thermal conductivity of  $\text{Ge}_{0.86}\text{Sb}_{0.08}\text{Bi}_{0.06}\text{Te}$  in the  $R3m$  phase.

DOI: [10.1103/PhysRevMaterials.5.114602](https://doi.org/10.1103/PhysRevMaterials.5.114602)

### I. INTRODUCTION

The group-IV monochalcogenides are currently considered promising materials for thermoelectric applications in the intermediate temperature range of 600–900 K. Among them, the high electrical conductivity of semiconducting germanium telluride GeTe has attracted a lot of interest, which has led to numerous studies [1–9] focused on improving the thermoelectric quantities of the material by doping onto the Ge sites. Different phonon engineering approaches have been employed in both experimental and theoretical studies to improve the thermoelectric properties of GeTe-based compounds [10–17]. GeTe crystallizes into a rhombohedral  $R3m$  symmetry, with an interaxial angle of  $57.5^\circ$  at room temperature [18,19]. The crystalline structure of GeTe may be viewed as being composed of two-atom-thick layers, marked the crystallographic basal  $a$ - $b$  plane, that are stacked along the axial  $c$  axis direction [Fig. 1(a)]. The noncentrosymmetric rhombohedral symmetry of GeTe allows the development of spontaneous ferroelectricity in the  $R3m$  phase [20,21]. Thermal displacement of the ions drives the GeTe to undergo a structural relaxation to form a high-symmetry cubic  $Fm\bar{3}m$  phase at  $\sim 670$  K, above which the ferroelectricity is lost [20]. GeTe is a  $p$ -type semiconductor, with high electrical conductivity  $\sigma$  contributed from the high hole carrier density, a high thermal conductivity  $\kappa$  comprised of a large contribution from the hole carriers, and a low Seebeck coefficient  $S$  [9]. Doping onto the Ge sites using Pb, Sb, Bi, or Ti has been shown [22–25] to be effective in lowering thermal conduc-

tivity and/or raising the Seebeck coefficient toward a higher thermoelectric figure of merit  $z \equiv S^2\sigma/\kappa$  that is currently used to mark the efficiency of heat-to-electricity conversion for thermoelectric materials [26–28]. An increase of  $zT$  from  $\sim 1$  for pristine GeTe  $\sim 700$  K to 1.3 has been found in the 6% Bi-doped  $\text{Ge}_{0.94}\text{Bi}_{0.06}\text{Te}$  melt ingots at 700 K [4]. A reduction of thermal conductivity by as much as 63% has recently been reported in  $\text{Ge}_{0.9}\text{Bi}_{0.1}\text{Te}$  crystals, giving a  $zT = 1.9$  at 740 K [8]. The degradation of thermal conductivity in Bi-doped GeTe was attributed to the alloying effect and lattice anharmonicity caused by Bi-doping [8]. In addition, Sb doping onto the Ge sites results in a reduction of thermal conductivity by a factor of  $\sim 2$ , giving a  $zT = 2.2$  for  $\text{Ge}_{0.92}\text{Sb}_{0.08}\text{Te}$  crystals at 740 K [9]. Inelastic neutron scattering (INS) measurements reveal harmonic dispersions for the acoustic phonons in GeTe as well as the appearance of an additional phonon band at an energy of 5–6 meV in  $\text{Ge}_{0.92}\text{Sb}_{0.08}\text{Te}$  [9]. One theoretical study of the phonon dynamics of Sb-doped GeTe suggested that the substitution of Sb onto Ge sites will significantly modify the phonon dispersion of pristine GeTe rather than affecting the electronic band structures [13]. However, the connection between the modification of the phonon modes and the reduction of thermal conductivity by the doping onto the Ge sites remains obscure.

To address this question, we carried out detailed INS measurements on a large  $\text{Ge}_{0.86}\text{Sb}_{0.08}\text{Bi}_{0.06}\text{Te}$  single crystal [weight 17.4 g, Fig. 1(b)] to provide direct information about the phonon dispersions, lifetimes, and propagation lengths, focusing on the rhombohedral  $R3m$  phase from 300 to 630 K. The codoping resulted in a reduction of thermal conductivity by a factor of 3.6 (from 4.0 to  $1.1 \text{ Wm}^{-1}\text{K}^{-1}$ ) at 650 K, giving a  $zT = 2.25$ . The INS measurements revealed a large

\*Corresponding author: [whli@phy.ncu.edu.tw](mailto:whli@phy.ncu.edu.tw)

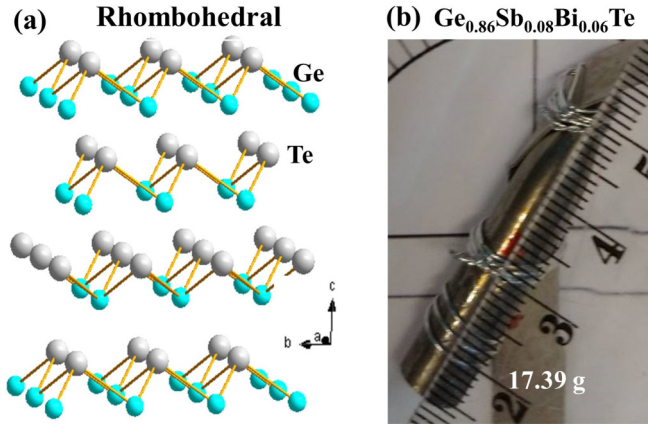


FIG. 1. Crystal structure and the single-crystal sample. (a) Crystal structure of GeTe in the rhombohedral  $R3m$  phase. (b) Photo image of the  $\text{Ge}_{0.86}\text{Sb}_{0.08}\text{Bi}_{0.06}\text{Te}$  single crystal used in this paper. The crystal weighed 17.39 g. The flat surface at the bottom indicates the  $a$ - $b$  plane in the cubic  $Fm\bar{3}m$ .

departure of phonon dispersion from the harmonic frequencies, with a downturn upon approaching the Brillouin zone boundary giving soft phonon energies at larger wave vectors. Two components that scatter lattice vibrations were found. A strong wave vector square  $q^2$  dependency linked to the electron-phonon coupling greatly softens the phonon energy, with thermal softening rate following the Fermi-Dirac thermal population reduction rate, and a linear wave vector  $q$  dependency which reflects the appearance of lattice anharmonicity from the three-phonon scattering interaction. The scattering of phonons is so strong that they propagate only over a few unit cells in length, with lifetimes as short as  $\sim 1$  ps.

## II. MATERIALS AND METHODS

### A. Preparation of $\text{Ge}_{0.86}\text{Sb}_{0.08}\text{Bi}_{0.06}\text{Te}$ single crystals

Single crystals of  $\text{Ge}_{0.86}\text{Sb}_{0.08}\text{Bi}_{0.06}\text{Te}$  were grown with a three-step process using the vertical Bridgman method. First, high-purity Ge, Sb, Bi, and Te shots (all 99.999% pure) were weighed using the stoichiometric ratio of  $\text{Ge}_{0.86}\text{Sb}_{0.08}\text{Bi}_{0.06}\text{Te}$ , then sealed in evacuated silica tubes under a high vacuum of  $10^{-6}$  Torr. The tubes were slowly heated to 1223 K at a rate of 150 K/h, then kept at 1223 K for 48 h, followed by furnace-cooling to room temperature. In the second step, the ingots thus obtained were crushed and sealed in a double silica tube, evacuated to  $10^{-6}$  Torr to avoid oxidation and fracturing. In the final step, the single crystal was grown employing the vertical Bridgman method, at a growth temperature of 1223 K and a slow growth rate of 3 mm/h. The cylindrical single crystal (8 mm in diameter and 50 mm in length with a needle-shaped end) used in the present measurements weighed 17.39 g [Fig. 1(b)] and had a mass density that is 2% away from the theoretical value.

### B. INS

Single-crystal neutron diffraction and inelastic scattering measurements were performed in the  $a$ - $b$  scattering plane at the Bragg Institute, ANSTO, using the cold neutron triple-axis

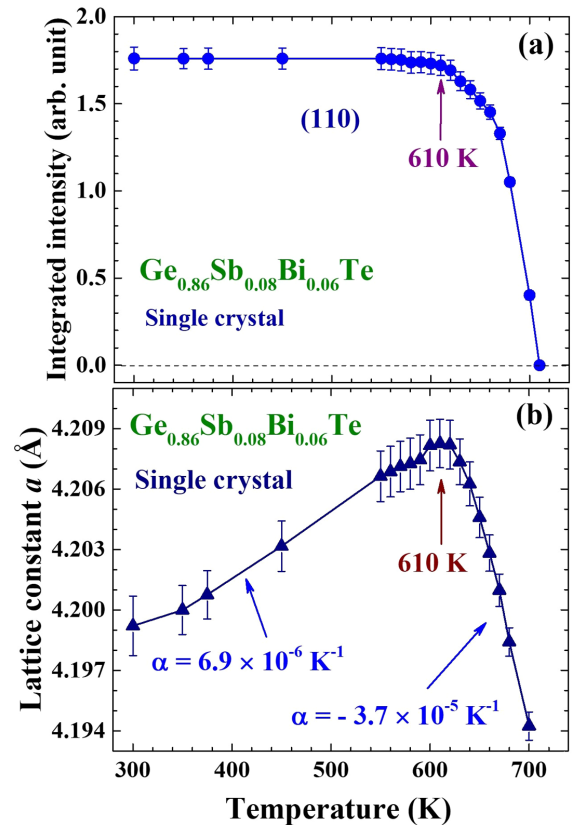


FIG. 2. Structural transition. (a) Temperature dependence of integrated intensity of the (110) Bragg reflection, measured with the crystal aligned for the (HK0) scattering plane of the  $R3m$  phase. Reductions of the intensity begin at 610 K before the disappearance of the Bragg reflection at 710 K. The dashed line indicates the base line for zero intensity. (b) Thermal variation of the lattice constant  $a$  reveals a relatively small thermal expansion coefficient  $\alpha = 6.9 \times 10^{-6} \text{ K}^{-1}$  from 300 to 610 K and a huge negative thermal expansion of  $\alpha = -3.7 \times 10^{-5} \text{ K}^{-1}$  in the transition region between 610 and 710 K.

spectrometer SIKA. The energy of neutrons was defined by PG(002) crystals at both the monochromator and analyzer positions, using a fixed final energy of 8.07 meV ( $\lambda = 3.18 \text{ \AA}$ ) and a cold Be filter to suppress higher-order contamination. The sample temperature was controlled using the CF-7 cryofurnace system, with the sample in a helium gas atmosphere. A slow heating rate of 10 K/min was employed to avoid possible breakage of the sample due to differences in the thermal expansion rates in the three crystalline axis directions, together with a 20 min wait time at the target temperature to allow the sample to reach thermal equilibrium.

## III. RESULTS

### A. Structural transition

The signature of the displacive phase transition from the  $R3m$  to the  $Fm\bar{3}m$  lattice of the crystal is marked by the disappearance of the representative (110) Bragg peak developed in the  $R3m$  phase. The rhombohedral  $R3m$  lattice begins to reconstruct into the cubic  $Fm\bar{3}m$  lattice at 610 K [Fig. 2(a)], accompanied by a large reduction in the lattice

constant [Fig. 2(b)], which continues until the structural transition is completed at 710 K at which the intensity of the (110) Bragg reflection reduces to zero. A relatively small thermal expansion of the lattice constant  $a$  with a linear expansion coefficient of  $\alpha = 6.9 \times 10^{-6} \text{ K}^{-1}$  is observed from 300 to 610 K, but it turns into a huge negative thermal expansion with  $\alpha = -3.7 \times 10^{-5} \text{ K}^{-1}$  in the transition region of 610 to 700 K [Fig. 2(b)]. No peak broadening but a progressive reduction in the intensity of the (110) Bragg reflection upon warming throughout the transition is found, showing the crystal is transforming from the rhombohedral  $R3m$  lattice to the cubic  $Fm\bar{3}m$  lattice portion by portion. The rhombohedral  $R3m$  lattice appears to coexist with the cubic  $Fm\bar{3}m$  lattice between 610 and 710 K. No thermal hysteresis of the structural transition was observed under temperature cycles in the transition regime, which is indicative of a second-order phase transition for the structural change.

### B. Phonon dispersion

INS measurement allows the mapping of phonon dispersions over the entire Brillouin zone and extraction of the phonon lifetime. The phonon lifetime  $\tau$  is related to the full width at half maximum  $W$  of the intrinsic excitation profile as  $\tau = (\pi W)^{-1}$  with  $\tau$  in units of picoseconds and  $W$  in terahertz [29]. We denote the neutron wave vector transfer  $\mathbf{Q}(Q_h Q_k Q_l) = \mathbf{G}(hkl) + \mathbf{q}(HKL)$ , where  $\mathbf{G}$  is a reciprocal lattice vector and  $\mathbf{q}$  the phonon wave vector. In these measurements, the crystal was aligned for the (HK0) scattering plane of the  $R3m$  phase, which allows the excess of the lattice vibrations along the crystallographic [110] direction. The small structure factor for the vibration along the [100] direction limits the excess to phonon excitation along the crystallographic  $a$ -axis direction.

Figure 3 shows the phonon excitations observed at 550 K in constant- $Q$  scans at four representative  $\mathbf{Q} = (110) + (\text{HH}0)$ . The peak widths of the two phonon excitations at  $E = 4.05$  and 4.96 meV, which appeared at  $H = 0.1$ , are much broader than the instrumental resolution, revealing a short lifetime of 1.18 ps for the transverse acoustic (TA) phonon at 4.05 meV and of 1.25 ps for the longitudinal acoustic (LA) phonon at 4.96 meV propagating along the [110] direction [open squares in Fig. 3(a)]. The TA and LA phonons shift to 7.23 and 10.81 meV, respectively, at  $H = 0.3$  [filled circles in Fig. 3(a)]. The energies of TA and LA phonons reduce to 6.69 and 11.15 meV, respectively, at  $H = 0.45$  [filled triangles in Fig. 3(b)] and a further reduction to 5.58 and 10.47 meV at  $H = 0.5$  [open diamonds in Fig. 3(b)]. Figure 4 displays the dynamic response function  $\chi''(\mathbf{Q}, E) = [1 - \exp(-E/k_B T)]S(\mathbf{Q}, E)$  at 450 K [Fig. 4(a)] and 550 K [Fig. 4(b)], covering from the Brillouin zone center at a scattering vector (110) to the zone boundary at (0.5,0.5,0) and extended to (0.4,0.4,0) of the next Brillouin zone, obtained by dividing the measured INS intensity  $S(\mathbf{Q}, E)$  by the Bose factor  $[1 - \exp(-E/k_B T)]^{-1}$ , where  $k_B$  is the Boltzmann constant. Two energy dispersions (dashed curves in Fig. 4) that belong to the TA and LA phonon branches are revealed in each of the intensity maps measured. The most distinct feature is the appearance of a downturn in each of the observed phonon dispersions, when the phonon wave vector reaches about two-thirds of the way to the zone boundary. The

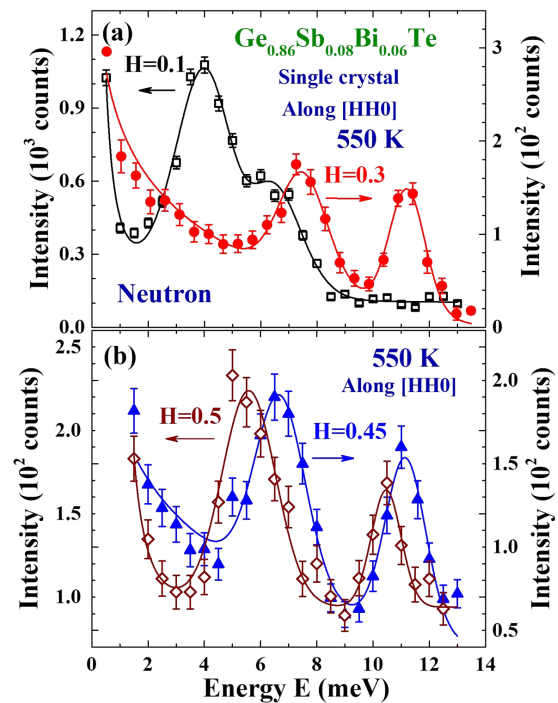


FIG. 3. Phonon excitation spectra. Phonon excitation spectra measured in constant- $Q$  scans along the crystallographic [HH0] direction at (a)  $H = 0.1$  (open squares) and 0.3 (filled circles) and (b)  $H = 0.45$  (filled triangles) and 0.5 (open diamonds) of the single-crystal  $\text{Ge}_{0.86}\text{Sb}_{0.08}\text{Bi}_{0.06}\text{Te}$  at 550 K.

amount of energy softening at the zone boundary is larger in the LA mode (21% in the LA mode and 12% in the TA mode at 450 K), and the downturn begins at a smaller wave vector.

The departure of the phonon energy from the harmonic frequency becomes larger at larger wave vectors upon shifting from the zone center toward the boundary [Figs. 5(a)–5(d)], showing the existence of an interaction that scatters phonons which is stronger at a larger wave vector. Assuming a  $q^n$  dependency for this interaction, with the exponent  $n$  as a fitting parameter, gives an  $n$  ranging from 1.84(7) to 2.02(8) for the 10 dispersions observed. It appears that the energy associated with the interaction can be described by a  $q^2$  dependency. In addition, an intrinsic component that specifies the appearance of lattice anharmonicity is also needed to describe the dispersions. We accordingly allow a  $q$  term plus a  $q^3$  term together with a  $q^2$  term for the dispersions but find a negligible coefficient for the  $q^3$  term ( $\sim 0.3\%$  of the harmonic term), which shows that the lattice anharmonicity can be described by a  $q$  dependency. The solid curves in Figs. 5(a)–5(d) indicate the results of the fitting of the data to  $E(q) = E_h \sin(q\pi) - E_a q - E_{e-p} q^2$ , where  $q$  is the wave vector in dimensionless reciprocal lattice units (r.l.u.);  $E_h$ ,  $E_a$ , and  $E_{e-p}$  are, respectively, the harmonic, anharmonic, and scattering energies at the zone boundary. All 10 phonon dispersions observed can be satisfactorily described throughout the entire Brillouin zone. The scattering energy  $E_{e-p}$  of the TA mode can be as much as 60% of the harmonic energy  $E_h$  [ $E_h = 13.0(3)$  meV and  $E_{e-p} = 7.80(9)$  meV at 300 K], reaching 43% in the LA mode [ $E_h = 18.3(3)$  meV and  $E_{e-p} = 7.92(9)$  meV at 300 K]. The anharmonic energy  $E_a$  is much

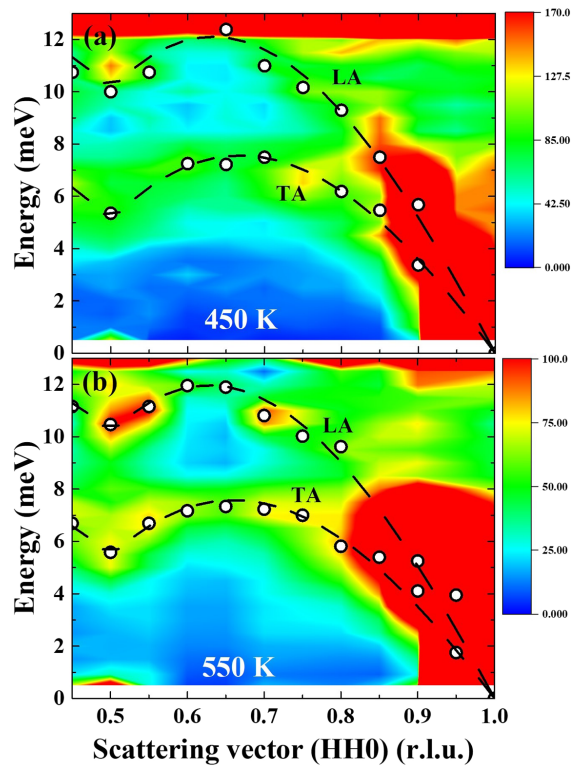


FIG. 4. Phonon dispersion maps in the  $R3m$  phase. Representative phonon excitation maps cover the entire Brillouin zone of  $\text{Ge}_{0.86}\text{Sb}_{0.08}\text{Bi}_{0.06}\text{Te}$  at (a) 450 K and (b) 550 K, measured in longitudinal scans along the crystallographic  $[\text{HH}0]$  direction. The circles indicate the peak positions obtained in each scan. Two energy dispersions (dashed curves) that belong to the transverse acoustic (TA) and longitudinal acoustic (LA) branches are revealed in each of the intensity maps.

smaller but clearly visible, softening  $\sim 10\%$  of the harmonic energy [1.33(4) meV for the TA mode and 1.21(4) meV for the LA modes at 300 K]. Note that assuming the existence of a  $q$  term for  $E_a$  improved the goodness for fits by 5–10% ( $\chi^2$  reduced from 0.1396 to 0.1327 for the LA mode at 300 K, from 0.1312 to 0.1227 for the LA mode at 550 K, from 0.585 to 0.532 for the TA mode at 450 K, and from 0.594 to 0.541 for the TA mode at 630 K). Existence of the  $q$  term in  $E(q)$  is also supported by the appearance of a small but nonzero intercept at the  $E$  axis in the observed  $\Delta E/\Delta q$ . The dispersions could not be described without the  $q^2$  term for  $E_{e-p}$ .

### C. Lattice anharmonicity

The harmonic energy  $E_h$  for the LA (open circles) and TA (open triangles) phonons decrease linearly with increasing temperature [Fig. 6(a)], showing that the softening of the phonon energy from thermal lattice expansion has been accounted for in the  $E_h$  obtained from the fits [30]. Here,  $E_{h0}$  is 20.6(7) meV for the LA phonons and 13.8(3) meV for the TA phonons, revealing that the harmonic coupling strength of the transverse phonons is  $(13.8/20.6)^2 = 45\%$  that of the longitudinal phonons. A small thermal reduction rate of  $\gamma = 6.8 \times 10^{-3}$  meV/K was obtained for the LA phonons, which amounts to a  $(6.8 \times 10^{-3} \times 330)/18.3 = 12\%$  softening

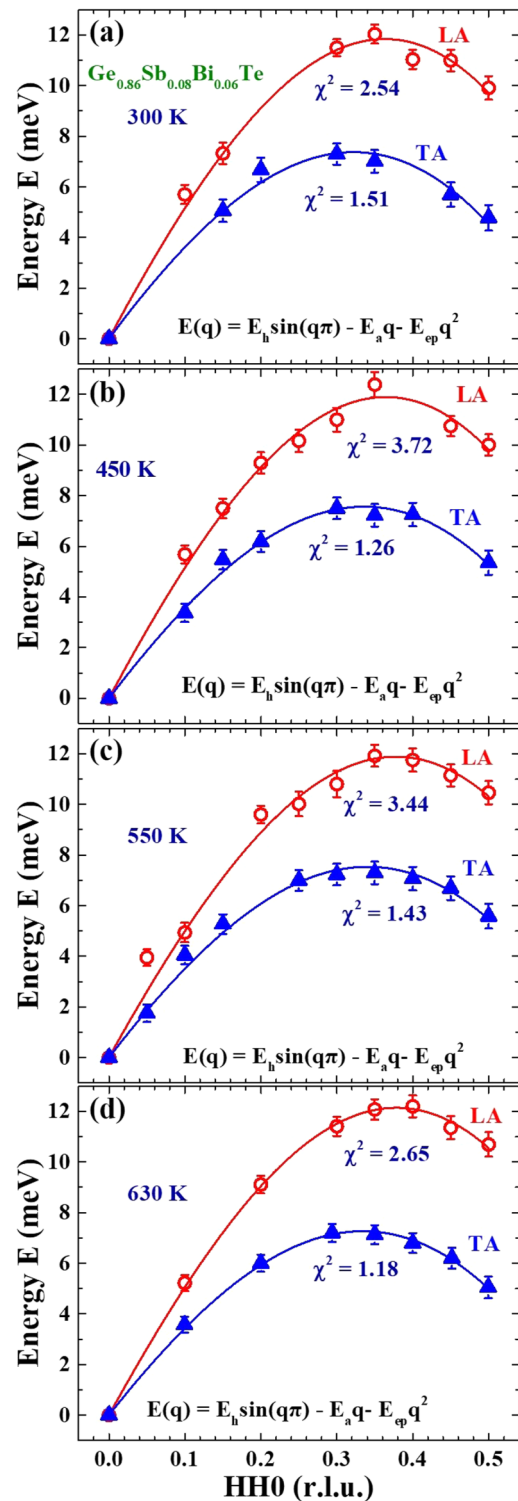


FIG. 5. Phonon dispersion. Phonon dispersion curves of  $\text{Ge}_{0.86}\text{Sb}_{0.08}\text{Bi}_{0.06}\text{Te}$  at (a) 300 K, (b) 450 K, (c) 550 K, and (d) 630 K along the crystallographic  $[\text{110}]$  direction. The solid curves indicate the results of the fits of the data to a harmonic term plus an anharmonic  $q$  term plus a scattering  $q^2$  term, as discussed in the text.

ing of the phonon energy upon warming from 300 to 630 K. The  $\gamma = 2.7(3) \times 10^{-3}$  meV/K for the TA phonons is a factor of 60% smaller. The small rate of thermal softening of the

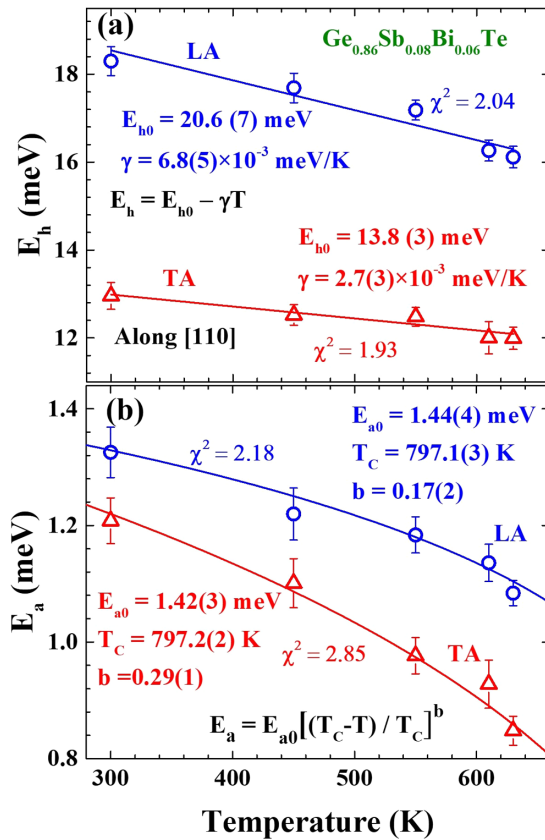


FIG. 6. Thermal variation of harmonic and anharmonic energies. Temperature dependencies of the (a) harmonic energy of longitudinal acoustic (LA) phonons (open circles) and transverse acoustic (TA) phonons (open triangles) and (b) anharmonic energy of LA phonons (open circles) and TA phonons (open triangles) of the Ge<sub>0.86</sub>Sb<sub>0.08</sub>Bi<sub>0.06</sub>Te crystal covering 300 to 630 K. The solid curves indicate the results of the fits of the data to the expressions listed in the plots.

phonon energy [Fig. 6(a)] is consistent with the small thermal lattice expansion coefficient of the lattice constant [Fig. 2(b)].

The temperature dependencies of the  $E_a$  for both the TA and LA phonons can be described by the critical expression of  $E_a = E_{a0} t^b$ , where  $t \equiv (T_c - T) / T_c$  is the reduce temperature for  $T < T_c$ ,  $b$  is the critical exponent,  $E_{a0}$  is the energy at zero temperature, and  $T_c$  is the temperature at which energy drops to zero. The  $E_a(T)$  curves obtained from the fits for both the LA and TA phonons give an  $E_{a0} = 1.43(5)$  meV and a  $T_c = 797(1)$  K, reflecting that they are linked to the same lattice vibration component [Fig. 6(b)]. Here,  $T_c = 797$  K indicates the temperature above which the lattice anharmonicity in the crystallographic [110] direction of the rhombohedral  $R3m$  phase would be thermally smeared if the lattice structure remains. Note that the rhombohedral  $R3m$  phase transfers into the cubic  $Fm\bar{3}m$  phase at 710 K. Here,  $E_a$  links to the three-phonon interactions that arise from the third-order atomic displacements [31]. The anharmonic energy  $E_{a0}$  amounts to 7% of harmonic energy  $E_{h0}$  for the LA phonons and 11% for the TA phonons. The thermal softening rate of  $E_a$  for the TA phonons is significantly larger than that of the LA phonons, characterized by a critical exponent of  $b =$

0.29(1) for the TA phonons and 0.17(2) for the LA phonons [Fig. 6(b)]. In the rhombohedral  $R3m$  phase, the Ge and Te ions crystallized into zigzag Ge-Te-Ge-Te-Ge-Te chains along the crystallographic [110] direction, where the atomic environment along the longitudinal and the transverse directions are different [Fig. 1(a)]. A larger thermal softening rate of  $E_a$  for the TA phonons, reflecting the thermal smearing rate of the third-order atomic displacement along the transverse direction is higher than that along the longitudinal direction. In addition, the thermal softening rate of  $E_a$  is considerably larger than that of  $E_h$  for the associated mode for both the TA and LA phonons [Figs. 6(a) and 6(b)]. Here,  $E_a/E_h$  weakens by 30% for the TA phonons and by 8% for the LA phonons upon increasing temperature from 0 to 630 K, revealing that thermal agitation has a stronger effect on the three-phonon interactions than on the harmonic couplings. Positive values for  $E_a$  were found, showing that the three-phonon interactions soften the phonon energy in the  $R3m$  phase.

#### D. Electron-phonon scattering

The scattering energy  $E_{e-p}$  is  $\sim 6$  times higher than the anharmonic energy  $E_a$ , reaching  $\sim 45\%$  of the harmonic energy  $E_h$ . Clearly, the  $E_{e-p}$  cannot arise from the higher-order multiple phonon-phonon scattering, but a mechanism stronger than phonon-phonon interaction must play a crucial role for the appearance of  $E_{e-p}$ . Another source of scattering that may occur is the electron-phonon interaction. The modification of the phonon energy from electron-phonon coupling can be expressed as [31]

$$\Delta E = - \sum_k |M_{kk'}|^2 \frac{2\langle n_k \rangle}{(E_{k'} - E_k)} \equiv -E_{e-p},$$

where  $M_{kk'}$  is the electron-phonon matrix element,  $E_k$  is the electron energy at wave vector  $k$ ,  $\langle n_k \rangle$  is the electron occupation number at wave vector  $k$ , and  $\mathbf{k} - \mathbf{k}'$  is the scattered wave vector which is equal to the phonon wave vector  $\mathbf{q}$ . The dependency of  $E_{e-p}$  on temperature appears mainly in  $\langle n_k \rangle$ . Heavily Bi- and Sb-doped GeTe belong to the degenerate semiconductors [8,9], where the donor band overlaps with the conduction band so that thermal population of electrons follows the Fermi-Dirac distribution [32]. Here,  $E_{e-p}$  is the scattering energy at the zone boundary, where the phonon wave vector has a specific value of  $q = 0.5$  r.l.u. Thermal variations of the observed  $E_{e-p}$  for both the LA and TA phonons can be described by a Fermi-Dirac thermal distribution:

$$\langle n_k \rangle \sim \frac{1}{\frac{1}{g} \exp(T_0/T) + 1},$$

where  $g$  is the degeneracy factor, and  $T_0$  indicates the energy of the scattered electrons in terms of temperature. The solid curves in Fig. 7 show the results of the fits to  $E_{e-p} = E_{e-p0} / \{[(1/g)\exp(-T_0/T)] + 1\}$  with  $E_{e-p0}$  indicates the electron-phonon coupling energy at zero temperature, assuming no thermal variation for  $g$ , revealing good agreements between the data and the fits. It is known that a  $q^2$  dependency is a characteristic of the conduction-electron energy dispersion together with  $E_{e-p}(T)$  following thermal variations of the conduction electron populations. We hence conclude that the

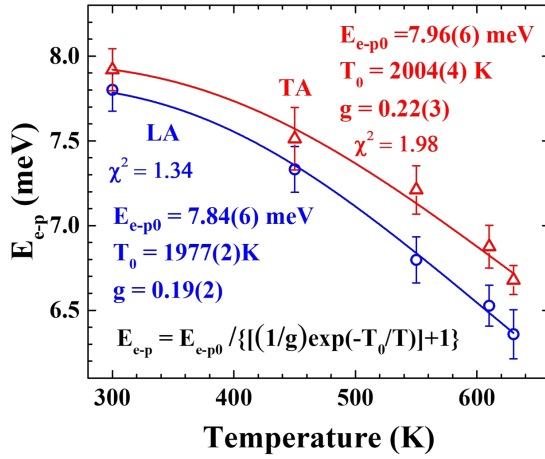


FIG. 7. Thermal variation of electron-phonon scattering energy. Temperature dependence of electron-phonon scattering energy of longitudinal acoustic (LA) phonons (open circles) and transverse acoustic (TA) phonons (open triangles) of the  $\text{Ge}_{0.86}\text{Sb}_{0.08}\text{Bi}_{0.06}\text{Te}$  crystal covering 300 to 630 K. The solid curves indicate the results of the fits of the data to the expressions listed in the plot.

$E_{e-p}$  comes from the electron-phonon interactions. A value of  $E_{e-p0} = 7.9(1)$  meV is obtained from the fits for both the LA and TA phonons (Fig. 7) even though the  $E_h$  of the LA mode is  $\sim 30\%$  higher than that of the TA mode [Fig. 6(a)], revealing that the electron-phonon coupling in the basal  $a$ - $b$  plane is weakly sensitive to the crystallographic direction. The value of the degeneracy factor reflects the fraction of conduction electrons participating in electron-lattice scattering. A slightly lower  $g = 0.19(2)$  for the LA phonons than the  $g = 0.22(3)$  for the TA phonons shows that the scattering rate of conduction electrons for the transverse vibrations is slightly higher than for the longitudinal vibrations. The smaller values of  $g = 0.19$  for LA phonons and  $0.22$  for TA phonons than the value of  $g = 2$  for the conduction electrons in donor level reflect only a small portion of the conduction electrons participating in electron-lattice scattering. A  $T_0 \approx 2000$  K (corresponds to 172 meV) was obtained for electrons scattered by LA and TA phonons at the zone boundary. Note that the electron-phonon coupling remains strong in the structural transition regime but weakens by  $\sim 16\%$  upon warming from 0 to 630 K.

### E. Phonon lifetime and propagation length

The widths of the phonon excitation profiles in the INS spectra are much broader than the instrumental resolution, revealing short propagation lifetimes for the phonons. The phonon excitation profiles can be described very well by Gaussian functions (solid curves in Fig. 3), which allow the extraction of observed peak widths and their uncertainty errors. Deconvolution of the observed width from the Gaussian instrumental resolution width allows extraction of the intrinsic width  $W$  of the excitation profiles for the calculation of associated lifetime by  $\tau = (\pi W)^{-1}$  with  $\tau$  in units of picoseconds and  $W$  in terahertz [29]. The uncertainty error of the observed width is used to calculate the upper and lower values of the lifetime for its uncertainty error. Lifetimes on the order of  $\sim 1.5$  ps for phonons propagating along the crystallographic

[110] direction at small wave vectors were found. Phonon lifetime shortens progressively with increasing wave vector from the zone center to the boundary, down to  $\sim 0.8$  ps at the zone boundary [Figs. 8(a) and 8(b)]. The lifetimes of the LA phonons are  $\sim 35\%$  longer than that of the corresponding TA phonons. This agrees with a stronger harmonic coupling [Fig. 6(a)] and a weaker electron-phonon coupling (Fig. 7) for the LA phonons. Shorter lifetimes for both the LA and TA phonons were found at higher temperatures. The phonon lifetimes shorten by  $\sim 30\%$  upon warming from 300 to 630 K.

Phonon group velocity  $V_g$  at a specific  $q$  can be calculated by  $V_g(q) = \Delta E / \Delta(\hbar q)$ . The group velocity is on the order of  $\sim 10^3$  m/s for the phonons near the zone center. The wave vector dependencies of the group velocity reveal a turning point at which the group velocities change from having positive values at small wave vectors to having negative values at larger wave vectors [Figs. 8(c) and 8(d)]. Here,  $E_h$ ,  $E_a$ , and  $E_{e-p}$  all increase with increasing  $q$ , but  $E_a$  and  $E_{e-p}$  result in softening of phonon energy. The turning point from a positive  $V_g$  to a negative  $V_g$  indicates the  $q$  value at which the increase of  $E_h$  from increasing  $q$  becomes smaller than the reduction from  $E_a$  and  $E_{e-p}$ , such that phonon energy shows a downturn to decrease upon increasing  $q$ . The turning point in the TA mode appears at a smaller wave vector of  $q \sim 0.3$  rather than the  $q \sim 0.37$  in the LA mode. The turning point shifts slightly to a larger  $q$  upon warming to higher temperatures (shifts from  $q = 0.3$  to  $0.33$  on warming from 300 to 630 K in the TA mode). The phonons with negative group velocities propagate toward the zone center and keep the propagation more localized [33]. These phonons are less effective in heat transport when compared with the phonons with positive group velocities. Given these lifetimes and group velocities, the propagation lengths of phonons can be calculated by  $l(q) = \tau(q) \times V_g(q)$ . The propagation of phonons in the  $R3m$  phase only extends over several unit cells, even for acoustic phonons propagating near the zone center, where the group velocities and phonon lifetimes are the highest [Figs. 8(e) and 8(f)]. The longest phonon propagation observed is  $l = 14.94 \text{ \AA}$  for the LA phonons at  $q = 0.1$  r.l.u. at 630 K, at which point phonon propagation extends over  $(14.94 \text{ \AA}) / (4.207 \times 1.414 \text{ \AA}) = 2.5$  unit cells long along the crystallographic [110] axis direction of lattice length  $4.207 \times 1.414 \text{ \AA}$ . The propagation length decreases progressively upon increasing  $q$  from the zone center to reach negative values around  $q \sim 0.3$  for the TA phonons and  $q \sim 0.35$  for the LA phonons. At the zone boundary, phonon propagation is limited to within 1 unit cell and toward the zone center. Short phonon propagation lengths limit heat transport, which gives rise to the desired poor thermal conductivity.

## IV. DISCUSSION

Huge electron-lattice scattering greatly softens the acoustic phonon energies in the  $R3m$  phase of the Sb/Bi codoped  $\text{Ge}_{0.86}\text{Sb}_{0.08}\text{Bi}_{0.06}\text{Te}$ . The electron-phonon scattering is so huge that it results in a downturn in the phonon dispersion to give smaller phonon energies at larger wave vectors toward the Brillouin zone boundary. No such downturn in phonon dispersion was detected in the 8% Sb-doped  $\text{Ge}_{0.92}\text{Sb}_{0.08}\text{Te}$ , but the energy of LA phonon at the zone boundary of  $q = 0.5$

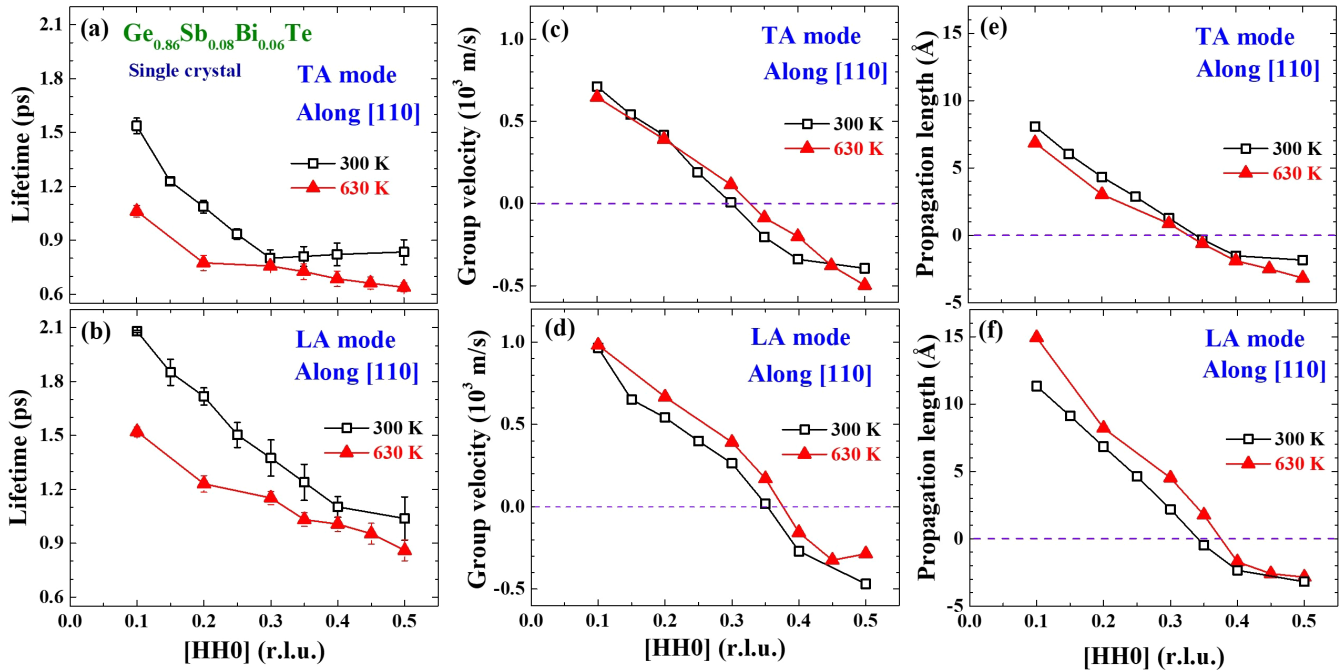


FIG. 8. Phonon lifetime, group velocity, and propagation length. Variation of (a) and (b) phonon lifetime, (c) and (d) group velocity, and (e) and (f) propagation length with wave vector across the Brillouin zone along the crystallographic [HH0] direction at two representative temperatures of 300 K (open squares) and 600 K (filled triangles). The solid curves are guides for the eye only.

was found to be lower than the energy at  $q = 0.4$  in the pristine GeTe [9]. Apparently, it is the codoping that triggers or greatly enhances electron-lattice interaction. The introduction of Bi onto the Ge sites plays an essential role in triggering or enhancing electron-lattice interaction.

Here,  $E_{e-p}$  reflects the electron-lattice coupling strength. The same  $E_{e-p0} \approx 7.9$  meV was obtained for scattering by the TA phonons as for the LA phonons (Fig. 7). Expressing  $E_{e-p0}$  in terms of the effective mass  $m^*$  of the electron using  $E_{e-p0} = \hbar^2 q^2 / 2m^*$  gives an  $m^*$  that is 861 times the free electron mass  $m_e$  for the electron-phonon coupling. The dimensionless electron-phonon coupling constant  $\alpha$  for quasi-two-dimensional  $\text{Ge}_{0.86}\text{Sb}_{0.08}\text{Bi}_{0.06}\text{Te}$  may then be calculated by  $m^* / m_e = 0.73\alpha^4$  [34], giving a value of  $\alpha = 5.86$  for the electron couples to the acoustic phonons propagating in the crystallographic [110] direction at zero temperature. The coupling constant  $\alpha$  increases to 6.11 for the TA mode and 6.19 for the LA mode at 630 K when calculated using the values of  $E_{e-p}$  obtained at 630 K. The thermal reduction rate of  $E_{e-p}$  is noticeably lower for TA phonon scattering, characterized by a larger degeneracy factor, showing that the strength of electrons coupled to TA phonons is less sensitive to thermal agitation than those coupled to LA phonons. The higher degeneracy factor observed for TA phonon scattering reveals a higher electron-phonon scattering cross-section for these electrons since the density of states of the electrons scattered by TA or by LA phonons at the zone boundary is similar [supported by the same  $T_0$  obtained from  $E_{e-p}(T)$  for the TA and LA phonons]. This apparently links to larger effective displacements of the ions in the TA phonons, where the ions vibrate within the basal  $a$ - $b$  plane, while the ions

are displaced at an inclined angle to the  $a$ - $b$  plane for the LA phonons in the Ge-Te-Ge-Te zigzag chains that extend through two-atom-thick layers.

## V. CONCLUSIONS

Neutron diffraction measurements reveal that the crystalline structure of Sb/Bi codoped  $\text{Ge}_{0.86}\text{Sb}_{0.08}\text{Bi}_{0.06}\text{Te}$  transforms from the  $R3m$  phase into the  $Fm\bar{3}m$  phase over a wide temperature range of 610–710 K, with the two structural phases coexisting in the transition region. INS measurements performed in the  $R3m$  phase, covering 300–630 K, reveal a large lattice anharmonicity together with a very strong electron-phonon interaction. At the Brillouin zone boundary, the energy of the lattice anharmonicity from multiple-phonon scattering reaches  $\sim 10\%$  of the harmonic energy, whereas the energy associated with the electron-phonon scattering reaches 60 and 43% of the corresponding harmonic energy of the TA and LA phonons, respectively. The strong electron-phonon scattering causes a huge softening of the phonon energies, extremely short phonon lifetimes on the order of 1 ps, extremely short phonon propagation lengths on the order of 5 Å, and negative group velocities for large wave vectors for acoustic phonons propagating in the crystallographic [110] direction. The very short phonon lifetimes are the origin of the low thermal conductivity observed. The very limited phonon propagation length, together with the negative phonon group velocity at large wave vectors, restricts heat transport, which explains the origin of the poor thermal transport because of a strong electron-phonon scattering in the  $R3m$  phase of  $\text{Ge}_{0.86}\text{Sb}_{0.08}\text{Bi}_{0.06}\text{Te}$ .

## ACKNOWLEDGMENTS

This paper was supported by the Ministry of Science and Technology of Taiwan under Grant No. MOST 110-2112-M-008-034. We acknowledge the Ministry of Science and

Technology of Taiwan for financial support through Grant No. MOST-108-2739-M-213-001 from the National Synchrotron Radiation Research Center (NSRRC) Neutron Cultivation Program in providing the neutron scattering facility used in this paper.

- [1] J. Davidow and Y. Gelbstein, Comparison between the mechanical and thermoelectric properties of three highly efficient *p*-type GeTe-rich compositions: TAGS-80, TAGS-85, and 3% Bi<sub>2</sub>Te<sub>3</sub>-doped Ge<sub>0.87</sub>Pb<sub>0.13</sub>Te, *J. Elec. Mater.* **42**, 1542 (2012).
- [2] Y. Gelbstein, J. Davidow, S. N. Girard, D. Y. Chung, and M. Kanatzidis, Controlling metallurgical phase separation reactions of the Ge<sub>0.87</sub>Pb<sub>0.13</sub>Te alloy for high thermoelectric performance, *Adv. Energy Mater.* **3**, 815 (2013).
- [3] D. Wu, L. D. Zhao, S. Hao, Q. Jiang, F. Zheng, J. W. Doak, H. Wu, H. Chi, Y. Gelbstein, C. Uher, C. Wolverton, M. Kanatzidis, and J. He, Origin of the high performance in GeTe-based thermoelectric materials upon Bi<sub>2</sub>Te<sub>3</sub> doping, *J. Am. Chem. Soc.* **136**, 11412 (2014).
- [4] S. Perumal, S. Roychowdhury, and K. Biswas, Reduction of thermal conductivity through nanostructuring enhances the thermoelectric figure of merit in Ge<sub>1-x</sub>Bi<sub>x</sub>Te, *Inorg. Chem. Front.* **3**, 125 (2016).
- [5] S. Perumal, P. Bellare, U. S. Shenoy, U. V. Waghmare, and K. Biswas, Low thermal conductivity and high thermoelectric performance in Sb and Bi codoped GeTe: Complementary effect of band convergence and nanostructuring, *Chem. Mater.* **29**, 10426 (2017).
- [6] J. Li, X. Zhang, Z. Chen, S. Lin, W. Li, J. Shen, I. T. Witting, A. Faghaninia, Y. Chen, A. Jain, L. Chen, G. J. Snyder, and Y. Pei, Low-symmetry rhombohedral GeTe thermoelectrics, *Joule* **2**, 976 (2018).
- [7] M. Hong, Z. G. Chen, L. Yang, Y.-C. Zou, M. S. Dargusch, H. Wang, and J. Zou, Realizing *zT* of 2.3 in Ge<sub>1-x-y</sub>Sb<sub>x</sub>In<sub>y</sub>Te via reducing the phase-transition temperature and introducing resonant energy doping, *Adv. Mater.* **30**, 1705942 (2018).
- [8] P.-C. Wei, C.-X. Cai, C.-R. Hsing, C.-M. Wei, S.-H. Yu, H.-J. Wu, C.-L. Chen, D.-H. Wei, D.-L. Nguyen, M. M. C. Chou, and Y.-Y. Chen, Enhancing thermoelectric performance by fermi level tuning and thermal conductivity degradation in (Ge<sub>1-x</sub>Bi<sub>x</sub>)Te crystals, *Sci. Rep.* **9**, 8616 (2019).
- [9] R. K. Vankayala, T.-W. Lan, P. Parajuli, F. Liu, R. Rao, S. H. Yu, T.-L. Hung, C.-H. Lee, S.-I. Yano, C.-R. Hsing, D.-L. Nguyen, C.-L. Chen, S. Bhattacharya, K.-H. Chen, M.-N. Ou, O. Rancu, A. M. Rao, and Y.-Y. Chen, High *zT* and its origin in Sb-doped GeTe single crystals, *Adv. Sci.* **7**, 2002494 (2020).
- [10] R. M. Murphy, É. D. Murray, S. Fahy, and I. Savić, Ferroelectric phase transition and the lattice thermal conductivity of Pb<sub>1-x</sub>Ge<sub>x</sub>Te Alloys, *Phys. Rev. B* **95**, 144302 (2017).
- [11] Y.-S. Song, J. Kim, and S.-H. Jhi, Phonon Instability and Broken Long-Ranged *p* Bond in Ge-Sb-Te Phase-Change Materials from First Principles, *Phys. Rev. Appl.* **9**, 054044 (2018).
- [12] Z. Liu, J. Sun, J. Mao, H. Zhu, W. Ren, J. Zhou, Z. Wang, D. J. Singh, J. Sui, C.-W. Chu, and Z. Ren, Phase-transition temperature suppression to achieve cubic GeTe and high thermoelectric performance by Bi and Mn codoping, *Proc. Natl. Acad. Sci. USA* **115**, 5332 (2018).
- [13] M. Hong, Y. Wang, T. Feng, Q. Sun, S. Xu, S. Matsumura, S. T. Pantelides, J. Zou, and Z.-G. Chen, Strong phonon-phonon interactions securing extraordinary thermoelectric Ge<sub>1-x</sub>Sb<sub>x</sub>Te with Zn-alloying-induced band alignment, *J. Am. Chem. Soc.* **141**, 1742 (2019).
- [14] L. Yue, T. Fang, S. Q. Zheng, W. L. Cui, Y. Wu, S. Y. Chang, L. J. Wang, P. P. Bai, and H. Z. Zhao, Cu/Sb codoping for tuning carrier concentration and thermoelectric performance of GeTe-based alloys with ultralow lattice thermal conductivity, *ACS Appl. Energy Mater.* **2**, 2596 (2019).
- [15] K. S. Bayikadi, C. T. Wu, L.-C. Chen, K.-H. Chen, F.-C. Chou, and R. Sankar, Synergistic Optimization of thermoelectric performance of Sb doped GeTe with a strained domain and domain boundaries, *J. Mater. Chem. A* **8**, 5332 (2020).
- [16] D. Dangić, É. D. Murray, S. Fahy, and I. Savić, Structural and thermal transport properties of ferroelectric domain walls in GeTe from first principles, *Phys. Rev. B* **101**, 184110 (2020).
- [17] Z. Guo, Q. Zhang, H. Wang, X. Tan, F. Shi, C. Xiong, Na Man, H. Hu, G. Liu, and J. Jiang, Bi-Zn codoping in GeTe synergistically enhances band convergence and phonon scattering for high thermoelectric performance, *J. Mater. Chem. A* **8**, 21642 (2020).
- [18] T. Chattopadhyay, J. X. Boucherle, and H. G. von Schnering, Neutron-diffraction study on the structural phase-transition in GeTe, *J. Phys. C: Solid State Phys.* **20**, 1431 (1987).
- [19] X. Q. Tran, M. Hong, H. Maeno, Y. Kawami, T. Toriyama, K. Jack, Z.-G. Chen, J. Zou, S. Matsumura, and M. S. Dargusch, Real-time observation of the thermally-induced phase transformation in GeTe and its thermal expansion properties, *Acta Mater.* **165**, 327 (2019).
- [20] M. J. Polking, M.-G. Han, A. Yourdkhani, V. Petkov, C. F. Kisielowski, V. V. Volkov, Y. Zhu, G. Caruntu, A. P. Alivisatos, and R. Ramesh, Ferroelectric order in individual nanometre-scale crystals, *Nature Mater.* **11**, 700 (2012).
- [21] U. D. Wdowik, K. Parlinski, S. Rols, and T. Chatterji, Soft-phonon mediated structural phase transition in GeTe, *Phys. Rev. B* **89**, 224306 (2014).
- [22] J. Li, X. Zhang, X. Wang, Z. Bu, L. Zheng, B. Zhou, F. Xiong, Y. Chen, and Y. Pei, High-Performance GeTe thermoelectrics in both rhombohedral and cubic phases, *J. Am. Chem. Soc.* **140**, 16190 (2018).
- [23] P. Li, T. Ding, J. Li, C. Zhang, Y. Dou, Y. Li, L. Hu, F. Liu, and C. Zhang, Positive effect of Ge vacancies on facilitating band convergence and suppressing bipolar transport in GeTe-based alloys for high thermoelectric performance, *Adv. Funct. Mater.* **30**, 1910059 (2020).
- [24] M. Li, M. Hong, X. Tang, Q. Sun, W.-Y. Lyu, S.-D. Xu, L.-Z. Kou, M. Dargusch, J. Zou, and Z.-G. Chen, Crystal symmetry induced structure and bonding manipulation boosting thermoelectric performance of GeTe, *Nano Energy* **73**, 104740 (2020).
- [25] Z. Liu, W. Gao, W. Zhang, N. Sato, Q. Guo, and T. Mori, High power factor and enhanced thermoelectric performance in Sb and Bi codoped GeTe: Insights into the hidden role of rhombohedral distortion degree, *Adv. Energy Mater.* **10**, 2002588 (2020).



- [26] M. S. Dresselhaus, G. Chen, M. Y. Tang, R. G. Yang, H. Lee, D. Z. Wang, Z. F. Ren, J.-P. Fleurial, and P. Gogna, New directions for low-dimensional thermoelectric materials, *Adv. Mater.* **19**, 1043 (2007).
- [27] L. E. Bell, Cooling, heating, generating power, and recovering waste heat with thermoelectric systems, *Science* **321**, 1457 (2008).
- [28] L. D. Zhao, V. P. Dravid, and M. G. Kanatzidis, The panoramic approach to high performance thermoelectrics, *Energy Environ. Sci.* **7**, 251 (2014).
- [29] G. Nilsson and G. Nelin, Phonon dispersion relations in Ge at 80 K, *Phys. Rev. B* **3**, 364 (1971).
- [30] S. W. Lovesey, *Theory of Neutron Scattering from Condensed Matters* (Clarendon Press, Oxford, 1984), pp. 124–125.
- [31] P. L. Taylor, *A Quantum Approach to the Solid State* (Prentice-Hall Inc, New Jersey, 1970), pp. 103–107, pp. 178–182.
- [32] N. W. Ashcroft, N. D. Mermin, and D. Wei, *Solid State Physics*, revised ed. (Cengage Learning Asia Pte Ltd, Singapore, 2016), pp. 771–773.
- [33] K. Tamm, T. Peets, J. Engelbrecht, and D. Kartofelev, Negative group velocity in solids, *Wave Motion* **71**, 127 (2017).
- [34] C. Grimaldi, Weak-and strong-coupling limits of the two-dimensional Fröhlich polaron with spin-orbit Rashba interaction, *Phys. Rev. B* **77**, 024306 (2008).